Vol. 18, No. 3 (2019) 1143-1160
Revista Mexicana de Ingeniería Química

EFFECT OF THE ROTATING REFERENCE FRAME SIZE FOR SIMULATING A MIXING STRAIGHT-BLADE IMPELLER IN A BAFFLED STIRRED TANK

EFECTO DEL TAMAÑO DEL MARCO DE REFERENCIA ROTATIVO PARA SIMULAR UN IMPULSOR DE MEZCLADO DE PALETAS RECTAS EN UN TANQUE CON BAFLES

A.D. De La Concha-Gómez[1], J. Ramírez-Muñoz[1]*, V.E. Márquez-Baños[2], C. Haro[1], A.R. Alonso-Gómez[3]
[1]*División de Ciencias Básicas e Ingeniería, Universidad Autónoma Metropolitana-Azcapotzalco, Av. San Pablo 180, Col. Reynosa Tamaulipas, CDMX, 02200, México.*
[2]*División de Ciencias Naturales e Ingeniería, Universidad Autónoma Metropolitana -Cuajimalpa, Av. Vasco de Quiroga 4871, Cuajimalpa de Morelos, Santa Fe Cuajimalpa, CDMX, 05348, México.*
[3]*CONACYT-Universidad Autónoma Metropolitana-Azcapotzalco, Av. San Pablo 180, Col. Reynosa Tamaulipas, Azcapotzalco, CDMX, 02200, México.*

Received: April 17, 2019; Accepted: June 6, 2019

Abstract

A computational fluid dynamics (CFD) study was performed to simulate the flow induced by a turbine of four flat blades in a stirred baffled-tank in laminar and turbulent flow regimes. The multiple reference frame approach is employed to model the impeller rotation. Laminar and standard $\kappa-\varepsilon$ turbulence models are used to simulate the fluid flow for Reynolds numbers below 115 and above 21000, respectively. The work focuses specifically on investigating the influence of the surface position separating the rotating reference frame (RRF) and the static reference frame (SRF) regions over the numerical results reliability. To this end, six cylindrical volumes are defined around the impeller and were used for varying the RRF size. Power number measurements were obtained to validate the CFD model. It was found that for laminar flow, the interface position between both regions does not have a substantial effect on numerical results. However, its position plays a substantial role as the flow regime increases; the higher this is, the larger the RRF must be. Finally, we employ the RRF-region dimensions obtained in turbulent conditions for reproducing satisfactorily experimental results of a published system.

Keywords: MRF approach, rotating reference frame, CFD simulations, stirred tank.

Resumen

Se realizó un estudio de dinámica de fluidos computacional (CFD, por sus siglas en inglés) para simular el flujo inducido por una turbina de cuatro paletas planas en un tanque agitado con bafles en régimen de flujo laminar y turbulento. Se empleó el enfoque de marco de referencia múltiple para modelar la rotación del impulsor. Se utilizó el modelo laminar y el turbulento $\kappa-\varepsilon$ standard para simular el flujo Newtoniano a números de Reynolds por debajo de 115 y por encima de 21000, respectivamente. El trabajo se centra específicamente en investigar la influencia de la posición de la superficie que separa el marco de referencia rotativo (RRF, por sus siglas en inglés) y la región del marco de referencia estático (SRF, por sus siglas en inglés) sobre la confiabilidad de los resultados numéricos. Con este fin, se definieron seis volúmenes cilíndricos alrededor del impulsor y éstos fueron usados para variar el tamaño de la región RRF. Se obtuvieron mediciones del número de potencia para validar el modelo CFD. Se encontró que para el flujo laminar, la posición de la interfaz entre ambas regiones no tiene un efecto sustancial en los resultados numéricos. Sin embargo, su posición juega un papel importante a medida que aumenta el régimen de flujo; cuanto más alto es, más grande debe ser el RRF. Finalmente, empleamos las dimensiones de la región RRF obtenidas en condiciones turbulentas para reproducir satisfactoriamente los resultados experimentales de un sistema publicado.

Palabras clave: enfoque MRF, marco de referencia rotativo, simulación CFD, tanque agitado.

1 Introduction

Food processing, polymer, biotechnological, painting and coating industries, among others, rely heavily on the efficient use of mixing tanks. Mixing processes are frequently carried out in baffled tanks at constant impeller speeds where increments in viscosity during different stages of some manufacturing processes, e.g., xanthan gum fermentation (Galindo and Nienow, 1992) and homogenization of water-based paints (Patton, 1979), could exceed four orders of magnitude. Thus, although it is a common practice to deal fluid mixing in the laminar to transitional flow regime

* *Corresponding author. E-mail*: jrm@correo.azc.uam.mx
https://doi.org/10.24275/uam/izt/dcbi/revmexingquim/2019v18n3/DeLaConcha
issn-e: 2395-8472

without the usage of baffles (Zalc *et al*., 2001; Ramírez-Gómez *et al*., 2015), it is possible to find baffled tanks operating at low Reynolds numbers corresponding to laminar creeping flow (Kelly and Gigas, 2003; Pakzad *et al*., 2013).

CFD techniques have become a useful tool to simulate laminar, transitional and turbulent flow in stirred tanks (Brucato *et al*., 2000; Van den Akker, 2006; Joshi *et al*., 2011a and 2011b; Fathi Roudsari *et al*., 2012; Ramírez-Muñoz *et al*., 2016; Ramírez-Muñoz *et al*., 2017; Mendoza *et al*., 2018; Tamburini *et al*., 2018; Ameur, 2018; Márquez-Baños *et al*., 2019). An important aspect to consider when performing simulations of baffled stirred-tanks is the modeling of the impeller rotation. To this end, different approaches have been proposed, among them, the Sliding-Mesh (SM) (Murthy *et al*., 1994) and the MRF (Luo, 1994) models are the most commonly used (Brucato *et al*., 1998; Lane *et al*., 2000; Deen *et al*., 2002; Murthy and Joshi, 2008; Fathi Roudsari *et al*., 2012).

In the SM approach, unsteady simulations are performed using two grid domains. One of them is attached to the rotating impeller and the other one to the stationary tank wall and baffles. The interaction between both domains is performed by interpolating the information across its interface at successive time-steps. The SM method is suitable for modeling with complete fidelity the impeller-baffle interaction; however, its computational cost is very high. On the other hand, for most current applications of interest, the impeller-baffle interaction is relatively weak; therefore, an unsteady flow field cyclically appears after a certain number of impeller rotations. This means that the relative position of the impeller with respect to the baffles is not essential, and steady-state simulations using the multiple reference frame (MRF) approach can be employed. Impeller-baffle interaction can be considered weak for dimensionless geometric ratios up to $D/T \approx 0.5$ (Oshinowo *et al*., 2000), where D and T are the impeller and the tank inner diameter, respectively.

In the MRF approach, the domain of the system is divided into two regions. The first, the RRF, is located in the inner part of the domain and consists of a cylinder-like surface enclosing the impeller. The reference frame in this domain is set to move at the same angular speed as the impeller. In the second one, i.e., SRF, which comprises the remainder domain, a laboratory reference frame is used (Luo, 1994). The transformation of the conservation equations into a rotating reference frame yields two additional terms (i.e., the centrifugal and Coriolis force) in the momentum equations. The results obtained in the RRF domain have to be coupled with the SRF domain through boundary conditions for all flow properties at the interface, and an iterative approach between both regions is required to achieve a converged solution (Sommerfeld and Decker, 2004).

The MRF method is much more computationally efficient than the SM model due to its steady-state calculations, its computational requirements is around one order of magnitude lower (Brucato *et al*., 1998; Lane *et al*., 2000). It has been reported that both results are comparable (Wechsler *et al*., 1999). MRF modeling has been intensively used in CFD simulations of stirred tanks operating at different flow regimes regimes (Deglon and Meyer, 2006; Glover and Fitzpatrick, 2007; Rahimi *et al*., 2010; Ammar *et al*., 2012; Sossa-Echeverria and Taghipour, 2012; Chtourou *et al*., 2014; Raffo-Durán *et al*., 2014; Devi *et al*., 2015; Ramírez-Gómez *et al*., 2015; Ramírez-Muñoz *et al*., 2016).

For stirred tanks operating in the turbulent regime, it has been pointed out that the selection of the surface position between RRF and SRF is not arbitrary. This has to be located where flow variables do not change appreciably either with azimuthal direction or with time, i.e., when an almost steady flow is established at this position (Sommerfeld and Decker, 2004). Oshinowo *et al*. (2000) suggested that the radial position of the interface between both zones for a single impeller (Rushton or pitched-blade turbine) is roughly midway between the impeller tip and the inner edge of the baffle. Furthermore, they carried out an analysis of the axial extents of the MRF interface by using the standard $\kappa - \varepsilon$, RNG $\kappa - \varepsilon$ and RSM models for simulating the turbulence. They found an influence of its position on the tangential velocity distribution. In their study, the MRF interface was set to ±R above and below the impeller for the radial flow Rushton turbine, while for the axial flow pitched-blade turbine, the MRF interface was set from ~R to ~4R, where R is the impeller radius.

Other MRF-oriented studies describing baffled-tanks stirred by a Rushton turbine where the position of the RRF domain is clearly defined are the works of Lane *et al*. (2000), Deglon and Meyer (2006) and Zadravec *et al*. (2007). Lane *et al*. (2000) set the interface position at an axial distance of ±0.5R from the impeller centerline, and radially at 1.5R. Deglon and Meyer (2006), based on experimental results reported by Lee and Yianneskis (1994), proposed that the extent of the RRF domain should be located

at a distance of half an impeller radius away from the impeller tip and 1.5 blade widths above and below the impeller. Zadravec *et al*. (2007), studied the influence of the RRF size. They defined four different cylindrical volumes around the Rushton turbine by varying the radial (~1.11R-1.43R) and axial dimensions (~0.62R-1.27R) of the cylindrical RRF region. They reported that, in order to obtain reliable numerical approximations of the flow field, the RRF region must be large enough as to include the point lying in the radial coordinate where the fluid motion shifts from accelerating to decelerating.

Direct numerical simulation (DNS) or large eddy simulation (LES) for complex geometries such as stirred tanks operating in the turbulent regime will require to employ the Sliding Mesh (SM) approach to proper modelling the impeller rotation with transient computations, resulting in prolonged periods of time computations while demanding large storage requirements. On the contrary, by conducting steady-state computations employing the MRF approach to account for the impeller-shaft rotation in addition to RANS-based turbulence models, considerable computing savings can be attained. MRF model can yield adequate results for flow field, mean velocity, pumping and power numbers predictions in stirred tanks, but different Reynolds Averaged Navier-Stokes (RANS) turbulence models (standard $\kappa-\varepsilon$, RNG $\kappa-\varepsilon$, the Reynolds stress, SST $\kappa-\varepsilon$, among others) generally under or over-predicts turbulence (Joshi *et al*., 2011b).

Deglon and Meyer (2006) demonstrated that at high Reynolds numbers, MRF approach and the standard $\kappa-\varepsilon$ model can accurately model turbulent flow with less computational effort provided that very fine grids coupled with higher-order discretization schemes are used. Based on this, in the case of the present study, the MRF method and the standard $\kappa-\varepsilon$ model are used.

MRF is well suited for modeling baffled stirred tanks operating in the laminar to transitional regimes (Kelly and Gigas, 2003; Pakzad *et al*., 2013). Despite the relevance of the RRF region, it turns out that there is no general consensus about its extent. To the best of the authors' knowledge, the role of the extent of the RRF region as a function of the flow regime has not been previously reported. This work focuses on investigate the influence of the axial and radial surface position separating the RRF and SRF on the numerical results of N_P and local velocity profiles in laminar and turbulent regimes.

2 Methodology

2.1 Experimental setup

The experimental equipment used in this work is presented in Figure 1a. It consists of a jacketed stainless-steel cylindrical tank with an inner diameter T=132 mm, with a dished bottom. The tank is equipped with four equally-spaced baffles of height H=110 mm, width J=13.2 mm, and thickness of 1 mm, hence, J/T=1/10. The offset between the tank wall and the baffles is of 5.72 mm. The ratios C/T and D/T, for which C represents the bottom off clearance measured from the impeller midplane, are set equal to 0.3848. The height (Z) at which the liquid interface remains at rest is equal to T, thus, Z/T=1, resulting in a fluid volume of 1.63 L. The studied impeller is a custom-made polylactic acid 3D-printed four flat-blade turbine. The impeller ratio D/W is set to 5, where W is the impeller width. Its other dimensions are shown in detail in Figure 1b.

Four different Newtonian fluids are used in the experiments. These consisted of three solutions prepared from a 45 °Bx food grade glucose and distilled water at mass glucose concentrations of 37.5% (fluid 1), 36.32% (fluid 2), 32.21% (fluid 3) and 0% (i.e., distilled water, Fluid 4), respectively. For fluids 1-3, viscosity values are obtained from rotational measurements at 23?C using an Anton Paar MCR 502 rheometer with concentric cylinder geometry, whilst their respective densities were measured by using a graduated cylinder and an analytical balance. Data for pure distilled water were obtained from Perry and Green (2008). Table 1 shows the density (ρ) and viscosity (μ) properties of the four employed fluids, the impeller rotational speed (N), as well as the impeller Reynolds number (Re= $\rho ND^2/\mu$) covered for the experimental power draw validations for each fluid.

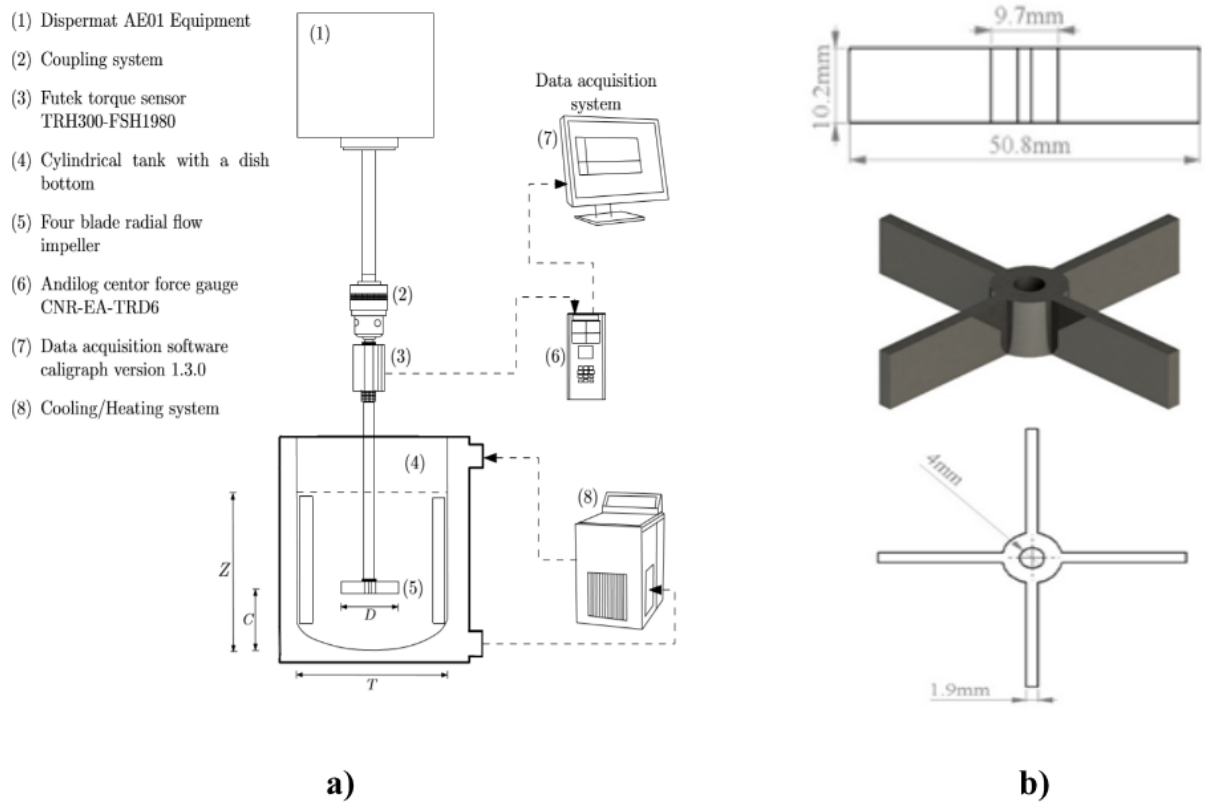

Fig. 1. a) Experimental setup, b) Scale drawing of the studied impeller.

Table 1. Fluids considered in this study.

Fluid	ρ(kg·m^{-3})	μ(Pa-s)	N interval (rpm)	Reynolds covered	
1	1365	2.4	40 - 1200	1 - 29.4,	laminar
2	1338	1.082	300 - 1500	16 - 79.8,	laminar
3	1317.4	0.4889	400 - 1000	46.4 - 115.9,	laminar
4	998.5	0.001	500 - 1000	21473 - 42946,	turbulent

In order to keep a constant fluid temperature of 23.0±0.5°C during all experimental runs, cooling (or warming) water is recirculated through the vessel jacket. Mechanical agitation of the shaft-impeller array is provided employing a user-controlled speed Dispermat® AE01 device (VMA-Getzmann GmbH, Germany) with 0.75 HP nominal power, where the impeller rotates in the clockwise direction. Torque measurements are performed using a Futek® TRH300-FSH1980 (Futek Advanced Sensor Technology, USA) data acquisition system attached directly to the shaft. This transducer has a maximum capacity of 6 N·m, a resolution of 6 mN·m and a full-scale precision of 0.5%. In our group (Ramírez-Muñoz *et al.*, 2017), this equipment has been previously used to reproduce adequately power number values reported by Rushton and Oldshue (1953) for a Rushton turbine operating in the laminar flow regime.

2.2 *Mathematical modelling*

The starting point for the computations conducted in this work are provided by the continuity and the Navier-Stokes equations for an incompressible flow.

$$\frac{\partial u_i}{\partial x_i} = 0, \tag{1}$$

$$\frac{\partial u_i}{\partial t} + \frac{\partial}{\partial x_j}(u_i u_j) = -\frac{1}{\rho}\frac{\partial p}{\partial x_i} + \nu \frac{\partial^2 u_i}{\partial x_j \partial x_i}, \tag{2}$$

where u_i and u_j are the velocity components in the i and j directions, respectively, ρ is the fluid density, p is the pressure and ν is the kinematic viscosity. In CFD, Eqs. (1) and (2) should ideally be solved directly

at any flow regime from laminar to turbulent, which would lead to a DNS modelling (Tamburini *et al*., 2018). Because of huge computational demands for turbulent flows, on most engineering problems dealing with turbulence, the statistical evolution of the flow in Eqs. (1) and (2) is then considered (Joshi *et al*., 2011b). From this, the well-known Reynolds averaged Navier-Stokes (RANS) equations are obtained (Pope, 2000):

$$\frac{\partial \overline{u}_i}{\partial x_i} = 0, \tag{3}$$

$$\frac{\partial \overline{u}_i}{\partial t} + \frac{\partial}{\partial x_j}(\overline{u}_i \overline{u}_j) = -\frac{1}{\rho}\frac{\partial \overline{p}}{\partial x_i} + \nu \frac{\partial^2 \overline{u}_i}{\partial x_j \partial x_i} - \frac{\partial}{\partial x_j}\overline{u_i' u_j'}. \tag{4}$$

In Eqs. (3) and (4), $\overline{u}_i$, $\overline{u}_j$ and u_i', u_j' are mean and instantaneous velocity components, respectively. The Reynolds stresses [term $\overline{u_i' u_j'}$ in Eq. (4)], which arises out of ensemble-averaging procedure can be modelled according to the Boussinesq hypothesis (Pope, 2000):

$$-\rho \overline{u_i' u_j'} = \mu_t \left(\frac{\partial \overline{u}_i}{\partial x_j} + \frac{\partial \overline{u}_j}{\partial x_i} \right) - \frac{2}{3}\rho \kappa \delta_{ij}, \tag{5}$$

where δ_{ij} is the Kronecker delta. In order to close the system of equations (3)-(5), the turbulent viscosity (μ_t) needs to be formulated. In the case of the present study, this was achieved by using the high Reynolds number standard $\kappa - \varepsilon$ closure model, which assumes the existence of isotropic turbulence and the spectral equilibrium (Pope, 2000). In the standard $\kappa - \varepsilon$ model, μ_t is estimated as:

$$\mu_t = \rho C_\mu \frac{\kappa^2}{\varepsilon}. \tag{6}$$

Where the turbulent kinetic energy (κ) and the rate of dissipation of turbulent kinetic energy (ε) for this study case (incompressible flow and isothermal conditions) are given by (Fluent, 2015)

$$\frac{\partial(\rho\kappa)}{\partial t} + \frac{\partial(\rho\kappa u_i)}{\partial x_i} = \frac{\partial}{\partial x_j}\left[\left(\mu + \frac{\mu_t}{\sigma_\kappa} \right) \frac{\partial \kappa}{\partial x_j} \right] + G_k - \rho\varepsilon, \tag{7}$$

$$\frac{\partial(\rho\varepsilon)}{\partial t} + \frac{\partial(\rho\varepsilon u_i)}{\partial x_i} = \frac{\partial}{\partial x_j}\left[\left(\mu + \frac{\mu_t}{\sigma_\varepsilon} \right) \frac{\partial \varepsilon}{\partial x_j} \right] + C_{1\varepsilon}\frac{\varepsilon}{\kappa} G_\kappa - C_{2\varepsilon}\rho\frac{\varepsilon^2}{\kappa} \tag{8}$$

Where G_k represents the generation of turbulence kinetic energy due to the mean velocity gradients. The model constants $C_{1\varepsilon} = 1.44$, $C_{2\varepsilon} = 1.92$, $C_\mu = 0.09$, $\sigma_\kappa = 1.0$ and $\sigma_\varepsilon = 1.3$ were used in simulations. These values have been determined from experiments, including frequently encountered shear flows like boundary layers, mixing layers and jets (Fluent, 2015, Joshi *et al*., 2011b).

Eq. (2) (laminar flow) or Eqs. (4), (7) and (8) (turbulent flow) can be further simplified by considering that the MRF approach is grounded on the assumption of steady state, this means that all derivatives with respect to time can be neglected. On the other hand, to account for the rotation of the inner domain in the MRF approach, two extra terms in Eqs. (2) and (4) have to be included, these are the Coriolis (F_{cor}) and centrifugal (F_{cent}) forces (Glover and Fitzpatrick; 2007), i.e.,

$$F_{cor} = -2\rho\boldsymbol{\omega} \times \mathbf{u} \tag{9}$$

and

$$F_{cent} = -\rho\boldsymbol{\omega} \times (\boldsymbol{\omega} \times \mathbf{r}). \tag{10}$$

Where, $\mathbf{u}$ is the velocity vector in an inertial reference frame, $\boldsymbol{\omega}$ is the angular velocity relative to an inertial reference frame, and $\mathbf{r}$ is the position vector pointing to the origin of the moving system.

2.3 *Computational mesh*

A digital model of the experimental system of Fig. 1 was reproduced using Ansys DesignModeler® module. The origin of the coordinate system was set at the impeller center. Considering that the system is periodic in the angular direction, only a fourth of the whole domain has been considered with the blade aligned with the baffle. If baffles are present, then it is not possible to reproduce adequately the real characteristics of the existing flow field by employing solely a single rotating frame that rotates along with the impeller. From this, the MRF approach was still used in laminar flow simulations where the impeller-baffles interactions are very weak. The MRF approach employed here resulted in the splitting of the entire domain of the system, yielding the SRF and RRF domains, as shown in the frontal view of Fig. 2.

In order to investigate the effect of the RRF size, this zone was further subdivided into seven volumes, as shown in the 2D and 3D details of Fig. 2. The innermost volume, the volume swept by the blades (BSV), is the existing volume of fluid delimited by the height and the length of the impeller blades. Volume V1 is the region immediately surrounding the BSV and the impeller. Volumes farther away than V1, i.e., from V2 up to V6, were successively defined enclosing the previous one. From this, all the components of the RRF domain were constructed as follows: RRF1=BSV+V1, RRF2=BSV+V1+V2, successively, up to RRF6=BSV+V1+V2+V3+V4+V5+V6. Each one of these volumes started at the shaft, but V1 is

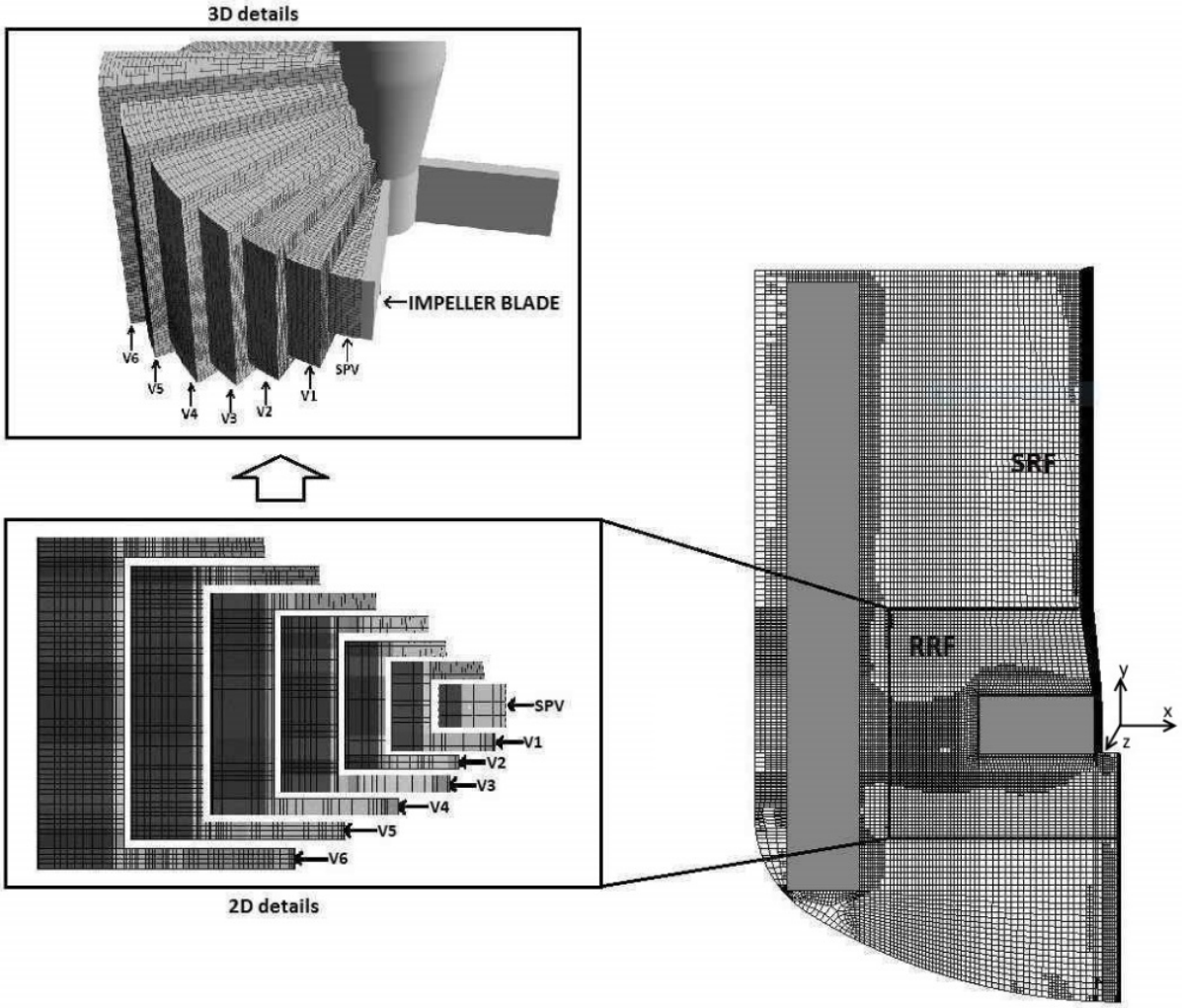

Fig. 2. Computational grid and different volume regions defined in the computational mesh.

peculiar in that its surface encloses BSV at a distance corresponding to W/3 in all directions. From V2 to V6 all the corresponding surfaces were located at a distance corresponding to W/4 from the previous one. This particular size of V1 was chosen by trial and error to avoid the formation of non-hexahedral cells throughout this region. The boundary between all regions, i.e., BSV, V1 to V6, and SRF, was conformal, meaning that all cell nodes comprising these boundaries were coincident between contact regions requiring no additional interpolation between adjacent regions.

Table 2 shows the dimensionless extensions of the six RRF regions considered in our CFD simulations, i.e., the radius and height of the cylinder enclosing the impeller, normalized by the impeller radius. For each computational mesh, volumes that were not part of the RRF, were included in the SRF region.

Table 2. RRF extents examined in this study.

Study case	RRF radius	RRF height
RRF1	1.133	0.669
RRF2	1.234	0.87
RRF3	1.334	1.07
RRF4	1.435	1.27
RRF5	1.535	1.472
RRF6	1.635	1.673

To ensure numerical accuracy while at the same time procuring computing effort as low as possible, an initial (coarsest) mesh, which consists exclusively of hexahedrons, was built in the ANSYS Meshing module. From this basic mesh, further refinement was conducted using ANSYS Fluent 17.1, and four meshes

Table 3. Different meshes considered and their corresponding number of elements for each fluid volume.

Mesh #	BSV	V1	V2	RRF V3	V4	V5	V6	SRF	Whole domain
1	3960	6408	8200	9992	11784	13576	15368	172020	241308
2	20760	32133	21276	20219	22004	23355	24881	239843	404471
3	31309	50515	54393	41443	29438	30019	39161	697370	973648
4	119782	102336	65271	78998	91010	100460	111744	1306594	1976195

with different densities and skewness below 0.88 were obtained (see Table 3). The refinement criteria employed was based on the maximum velocity gradients obtained at the highest Re number evaluated in this study (Re=42946).

2.4 Numerical considerations

It is generally accepted in the literature that for Re≥10000 the flow in a stirred tank can be considered as fully turbulent, whereas the laminar flow regime is limited to impeller Re around 10 (Paul *et al*., 2004; Gibbardo *et al*., 2006). Whilst the flow between the above two Re can be considered to be in the transitional flow regime.

For Re around 100, the transient flow range is closer to the laminar regime, and therefore, it is common to conduct simulations in the laminar flow regime (Zalc *et al*., 2001; Gibbardo *et al*., 2006; Pakzad *et al*., 2013; Ramírez-Muñoz *et al*., 2016; Mendoza *et al*., 2018). Ramírez-Muñoz *et al*. (2016) numerically studied the flow field induced by a standard Rushton turbine up to Reynolds number of 125 and evaluated the effect of the κ-κl-omega transition model introduced by Walters and Cokljat (2008). They reported that this model yields values of turbulent energy dissipation in the RRF region of at least five orders of magnitude lower than the viscous energy dissipation. From this, in the present study, we use laminar model for Re<125 and turbulent $\kappa - \varepsilon$ model for Re>21000.

In the study conducted by Deglon and Meyer (2006), a very fine grid consisting of nearly 2 million cells in one-half of the circumferential domain of a 15 cm diameter stirred tank was required to predict accurately the turbulent kinetic energy up to Re= 60,000. In the present study, an independent mesh of nearly one million cells is used in one-fourth of the circumferential domain of a 13.2 cm diameter cylindrical tank for simulations up to Re= 42,946. In addition, Deglon and Meyer?s (2006) considerations are followed for CFD simulations in the turbulent flow regime, namely (1) the standard $\kappa - \varepsilon$ turbulence model with standard model constants, (2) the QUICK discretization scheme, (3) the standard wall functions, (4) the standard pressure-velocity scheme together with the SIMPLEC algorithm.

On the other hand, for Re≤115.9, the laminar model was used. At this flow regime, Ramírez-Gómez *et al*. (2015) considerations are followed in the simulations: (1) The discretization scheme considered was QUICK, and (2) the standard pressure-velocity scheme together with the Coupled algorithm was employed.

In all simulations, non-slip boundary conditions were applied to all solid surfaces of the system (shaft, impeller, baffles and tank walls). At the liquid surface, a zero-shear stress condition was specified. The shaft and the impeller were considered moving walls with the same rotating velocity as the RRF, whereas the baffles, vessel walls, tank bottom and the SRF region, were considered static.

To simulate this system, Ansys Fluent© 17.1 software was used and steady-state numerical simulations were performed. The solutions were considered converged when the average of the computed torque values along the impeller-shaft over the previous 500 iterations did not exhibit variations beyond 0.1% and the largest values of the residuals for the continuity and momentum equations remained constant with a value below 10-4.

3 Results and discussion

3.1 Mesh independence analysis and numerical validations

For the purpose of corroborating that simulation results are independent of the mesh density, four grids of different densities, ranging from 241308 to 1976195 elements were built, as shown in Table 3. For this analysis, only the largest rotating domain was considered as the RRF, thus, RRF=RRF6. To capture the flow details where the highest velocity gradients

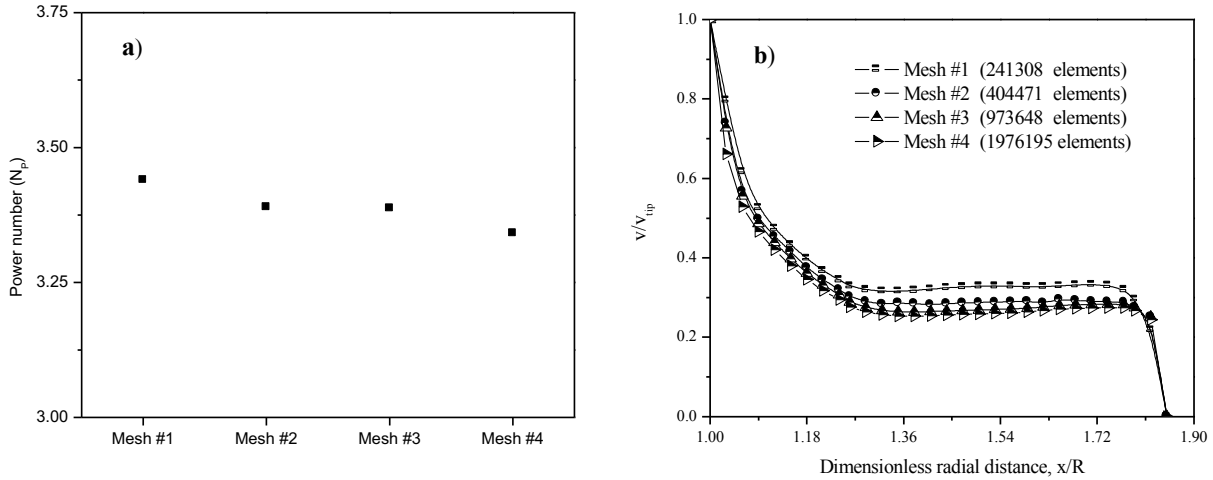

Fig. 3. Mesh independence analysis at Re=42946, using RRF=RRF6. (a) Numerical power number values. (b) Normalized velocity magnitude as function of the dimensionless radial distance.

exist, special attention was devoted to regions nearest to the impeller, baffles and tank wall. Thus, a higher refinement in the number of mesh elements was used in these fluid regions (see Fig. 2).

The power number was computed from torque measurements as follows:

$$N_P = \frac{2\pi\Im}{\rho N^2 D^5}. \tag{11}$$

Where, $\Im$ is the torque on the shaft and the impeller. Owing to the system periodicity, numerical torque values were multiplied by a factor of four.

N_P values for the four different evaluated meshes are presented in Fig. 3a. In Fig. 4b, numerical velocity magnitude values for the four mesh densities are compared. These values were extracted along a radial line connecting the impeller tip to the inner edge of the baffle and then they were normalized with respect to the impeller tip velocity (v_{tip}).

It is clear that if only N_P values over the entire domain of the system were used for the mesh independence analysis (Fig. 3a), the mesh that could be considered independent would be Mesh #1, because its difference with respect to the densest mesh (Mesh #4) is less than 3%. However, it is clear from Fig. 3b that there are still significant discrepancies in the local velocity profiles between them. On the previous basis, it was decided that Mesh #3, with 973648 elements, might be considered independent, and was used in further simulations. With this selection, numerical differences in N_P between Mesh #3 and the densest mesh are less than 1.5%, and there is a good agreement between the velocity magnitude profiles of both.

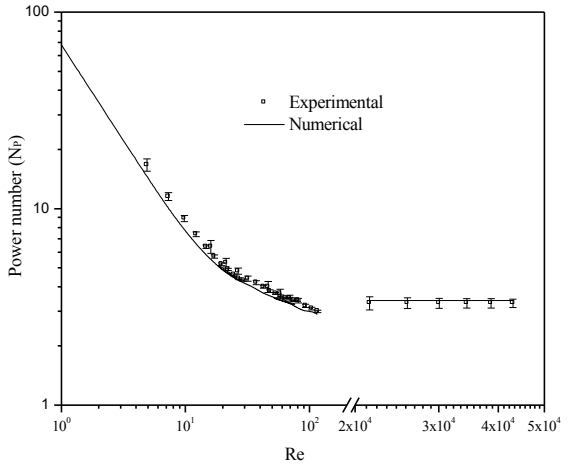

Fig. 4. Comparison between experimental and numerical power number values.

To validate the simulation results for the selected independent mesh, numerical N_P values using RRF=RRF6 were compared with those obtained experimentally. Results are included in Fig. 3. In general, a reasonable agreement between experiments and numerical values is observed. A maximum error of 13.2% was obtained at Re=4.9, which could be attributed to the closeness of the torque readings to the resolution of the device at this Re. For this reason, experimental Reynolds numbers below 4.9 were not consider in this study. The standard deviation over 100 experimental N_P readings at each Re value is indicated as error bars in Fig. 4. It should be noted that a break in Re between 120 and 20000 was included in this figure.

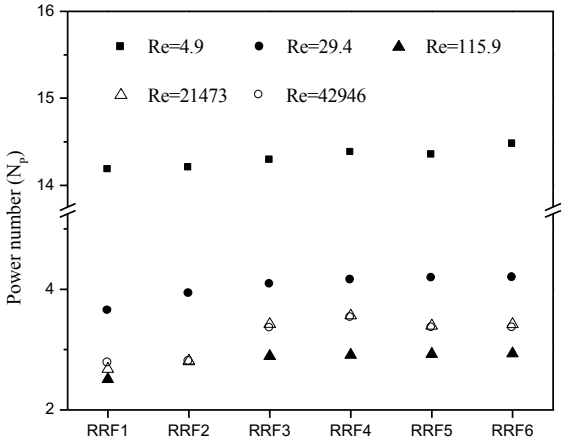

Fig. 5. Numerical power number as a function of the size of the RRF region.

3.2 *RRF-region size effect on numerical N_P values*

Fig. 5 shows numerical N_P values when the size of the RRF region is increased from RRF1 to RRF6 for five different Re numbers evaluated. Overall, it can be seen that, except for the lowest Re of 4.9, there is an effect of the size of the RRF region on the computed N_P values. This particular result suggests that for laminar flow it suffices that the extent of the RRF region equals that of RRF1. However, as Re increases, it becomes evident that an increment in the size of the RRF domain should be used to reduce the differences in N_P data between consecutive dimensions of the RRF, but also with respect to the largest RRF dimension (RRF6). For instance, at Re=29.4 an initial 13% difference in the computed N_P value between RRF1 and RRF6 is reduced to less than 4% between RRF3 and RRF6. In the case of Re=115.9, this criterion is also fulfilled when the RRF domain coincides with RRF3. A larger size of the RRF needs to be considered for turbulent flow conditions, where the extent of the RRF region must be enlarged to RRF5.

It is worth noting that for Re=42946, corresponding to the turbulent flow regime, important information can be deduced when numerical N_P values computed as a function of the number of elements for the mesh considered in this study (Fig. 3a) are compared with those obtained by varying the size of the RRF (Fig. 5). In the case of Fig. 3a, N_P variations not greater than 3% are obtained when the coarsest mesh (Mesh #1) is compared with the densest mesh (Mesh #4). In contrast, a difference of 17% is present in the N_P computed value between RRF1 and RRF6. This result suggests that, for the computational meshes evaluated in this study, numerical N_P values are more sensitive to changes in the extension of the RRF region, than to the increase in the number of elements of the mesh. It is worth mentioning that the maximum increment in the computation time incurred by approximating the additional Coriolis and centrifugal force terms, which arise in the momentum equation when the rotating domain increases from RRF1 to RRF6, was obtained from turbulent flow simulations. However, this was lower than 2%, and therefore, were regarded as insignificant.

3.3 *RRF-region size effect on local velocity magnitude profiles and shear rates*

Fig. 6 shows normalized values of the velocity magnitude as a function of the dimensionless axial distance (y/R) for the six different sizes of the RRF region. These values were extracted from simulation results along a vertical line over 50 points evenly spaced. This line connects the bottom of the tank with the free surface of the liquid and passes through the impeller tip (i.e., x=R), as can be seen in Fig. 6a. Black-filled triangles in the top of each figure indicate the respective axial location above and below the impeller midplane of each evaluated RRF-region. They indicate the vertical interface positions separating the RRF and SRF regions as the RRF domain increases its size. Overall, it can be seen that for low to moderate Reynolds number (Re of 4.9, 29.4 and 115.9), no significant effects can be observed over these numerical approximations along the vertical line by varying the size of the RRF region. Only small differences located near the edges of the impeller blade (y/R$\approx \pm 0.3$) are present for these computed values at Re=115.9 (Fig. 6c) when the RRF region is smaller than RRF3. Figs. 6d and 6e show results for Re=21473 and Re=42946, respectively. In these cases, it is clear that there is an effect on the velocity magnitude values when the size of the RRF region varies between RRF1 and RRF4.

The previous results concerning the velocity magnitude values evaluated along a vertical line at x=R (see Fig. 6a), suggest that reliable numerical approximations will be obtained independently of the Reynolds numbers as long as its dimensions are established between the interval whose lower and upper bounds are delimited by RRF5 and RRF6, respectively.

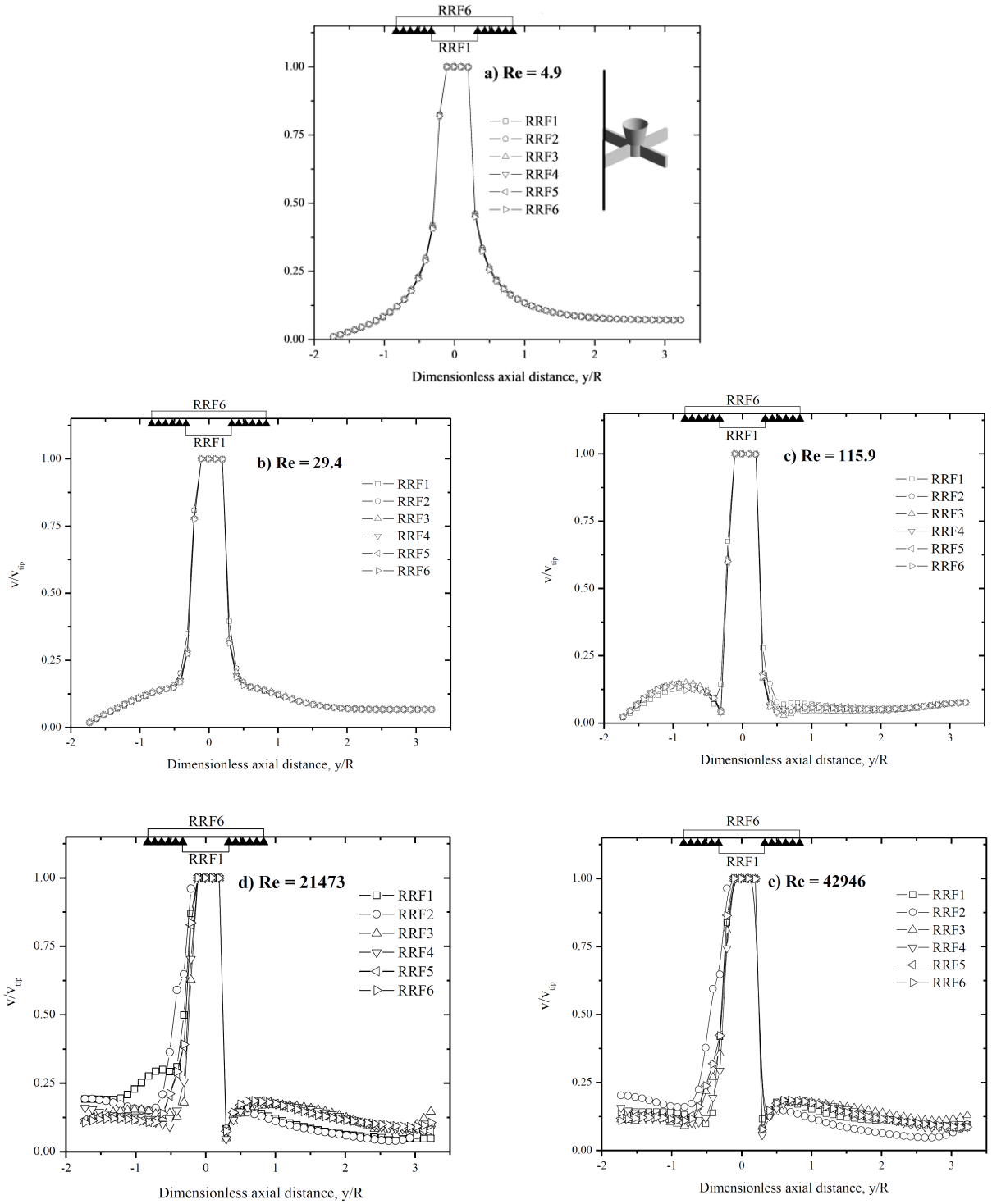

Fig. 6. Dimensionless velocity magnitude along an axial line at x=R for Re: a) Re=4.9, b) 29.4, c) Re=115.9, d) Re=21473 and e) Re=42946.

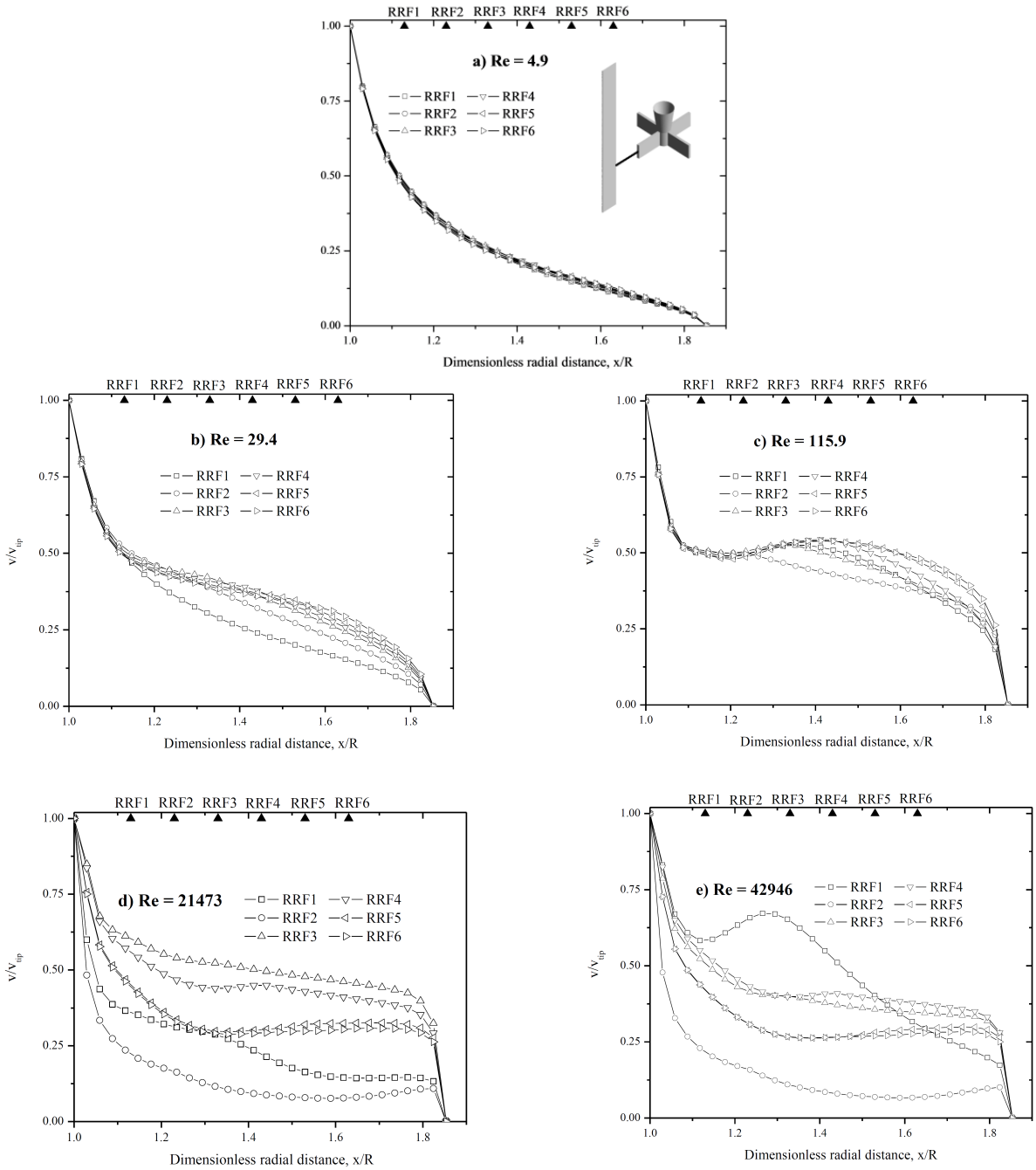

Fig. 7. Dimensionless velocity magnitude along a radial line at y=0 (impeller midplane) for Re: a) Re=4.9, b) 29.4, c) Re=115.9, d) Re=21473 and e) Re=42946.

Fig. 7 presents normalized values of the velocity magnitude computed over 30 points evenly spaced along a radial line. This line connects the impeller tip with the inner edge of the baffle (see Fig. 7a). Above each figure, the respective radial locations from RRF1 to RRF6 are also indicated. They correspond to the interface position separating the RRF and SRF regions as the RRF domain grows.

At Re=4.9 (Fig. 7a), it can be confirmed that there is a good agreement between velocity profiles

computed as a function of the extension of the RRF. At this, the lowest Re investigated, results suggest that an extension of the RRF equal to that of RRF1 will provide reliable approximations.

In the case of Re=29.4 (Fig. 7b), it can be seen that the velocity magnitude profiles are dependent on the size of the RRF region, being RRF1 and RRF2 the cases for which there exist the highest differences with respect to larger RRF regions. However, if the interface separating the RRF and SRF domains is placed at the distance of RRF4 or greater, there will be good agreement between the velocity magnitude profiles. A similar scenario can be established for the case of Re=115.9; however, the size of the RRF must be extended to RRF5.

In the cases of turbulent flow regime (Re of 21473 and 42946, Figs. 7d and 7e, respectively), for extensions up to RRF4, the velocity magnitude profiles show no clear behavior with respect to those obtained from RRF6. However, if the size of the RRF domain is grown to RRF5, i.e., a radial and axial extensions of 1.54R and 1.47R, respectively, a good correspondence can be established between both velocity profiles. This radial extension is in agreement with that of 1.5R proposed by Lane *et al*. (2000) and Deglon and Meyer (2006), although larger than 1.17R (i.e., equivalent to the midpoint between the impeller tip and the inner edge of the baffle) as was employed by Oshinowo *et al*. (2000). In our study case, the obtained axial extension (1.47R) of the RRF region is greater than those used by Lane *et al*. (2000) and Deglon and Meyer (2006), whom employed, one impeller radius (R) and 1.2R, respectively, however it turned out to be smaller than 2R set by Oshinowo *et al*. (2000). On the other hand, the largest radial and axial extensions evaluated by Zadravec *et al*. (2007) of 1.4R and 1.3R, respectively, are smaller than those found in the present study.

The observed effect of the RRF size on the numerical velocity magnitude profiles along the radial direction may be attributed to the following facts: 1) the use of a radial flow impeller in this study, since the highest velocity gradients exist in this direction; 2) the impeller region of influence (i.e. the circulating flow around the impeller) extends as the Re increases (Mendoza *et al*., 2018), and therefore, the radial extension of the RRF region must be extended as well.

Comparing Figs. 3b and 7e, it is clear that, in analogy with N_P values discussed before, the velocity magnitudes from simulation results are less sensitive to the number of elements in the computational mesh than to the size of the RRF region. Therefore, an adequate selection of the size of the RRF is crucial for modeling the impeller rotation with the MRF approach, since the resulting velocity profiles along the radial direction are very sensitive to its size.

On the other hand, a hydrodynamic parameter that plays a significant role in the evaluation of the impeller performance in industrial mixing processes is the shear rate (Wu and Patterson, 1989). For instance, the shear rated induced by the impeller near its blades swept volume has been related to cell damage (McFarlane and Nienow, 1995), enzyme inactivation (Ghadge *et al*., 2005), liquid-liquid dispersions (Paul *et al*., 2004) and breaking of particle agglomerates (Ramírez-Muñoz *et al*., 2016). Therefore, the ability of accurately compute its magnitude in the impeller proximities will play a key role in the optimal design of a wide variety of mixing processes.

In Fig. 8 are showed average shear rate values extracted from simulations in regions near the impeller (BSV and from V1 to V4, see Figure 2) as a function of the RRF-region size: Re=4.9 (Fig. 8a), Re=115.9 (Fig. 8b) and Re=42946 (Fig. 8c). Results show that, for laminar and turbulent regimes, maximum shear rate values are located near the impeller, i.e., in BSV and V1. However, at Re=4.9, its maximum value is located in V1, whilst at Re of 115.9 and 42946, maximum values of shear rate induced by the impeller are located in the blades swept volume (BSV). It should be noted that the similitude in the average shear rate values induced by the impeller at Re of 115.9 and 42946 comes from the fact that for both Reynolds number the same impeller speed (1000 rpm) was used (see Table 1).

With regards to the effect of the size of the RRF region, it can be seen that for Re=4.9, there is no effect of its size on the computed average shear rate values. For Re=115.9, RRF1 and RRF2 are the extensions for which there exist the highest differences with respect to larger RRF regions in BSV, V1 and V2; whilst, for the case of Re=42946; the size of the RRF must be extended to RRF5.

The results obtained show that for reliable numerical approximations, the RRF domain must correspond to RRF5 (radial and axial dimensions of 1.54 and 1.47 impeller radius, respectively), to prevent discrepancies in the computed values of N_P, velocity profiles and average shear rates near the impeller, regardless of the flow regime.

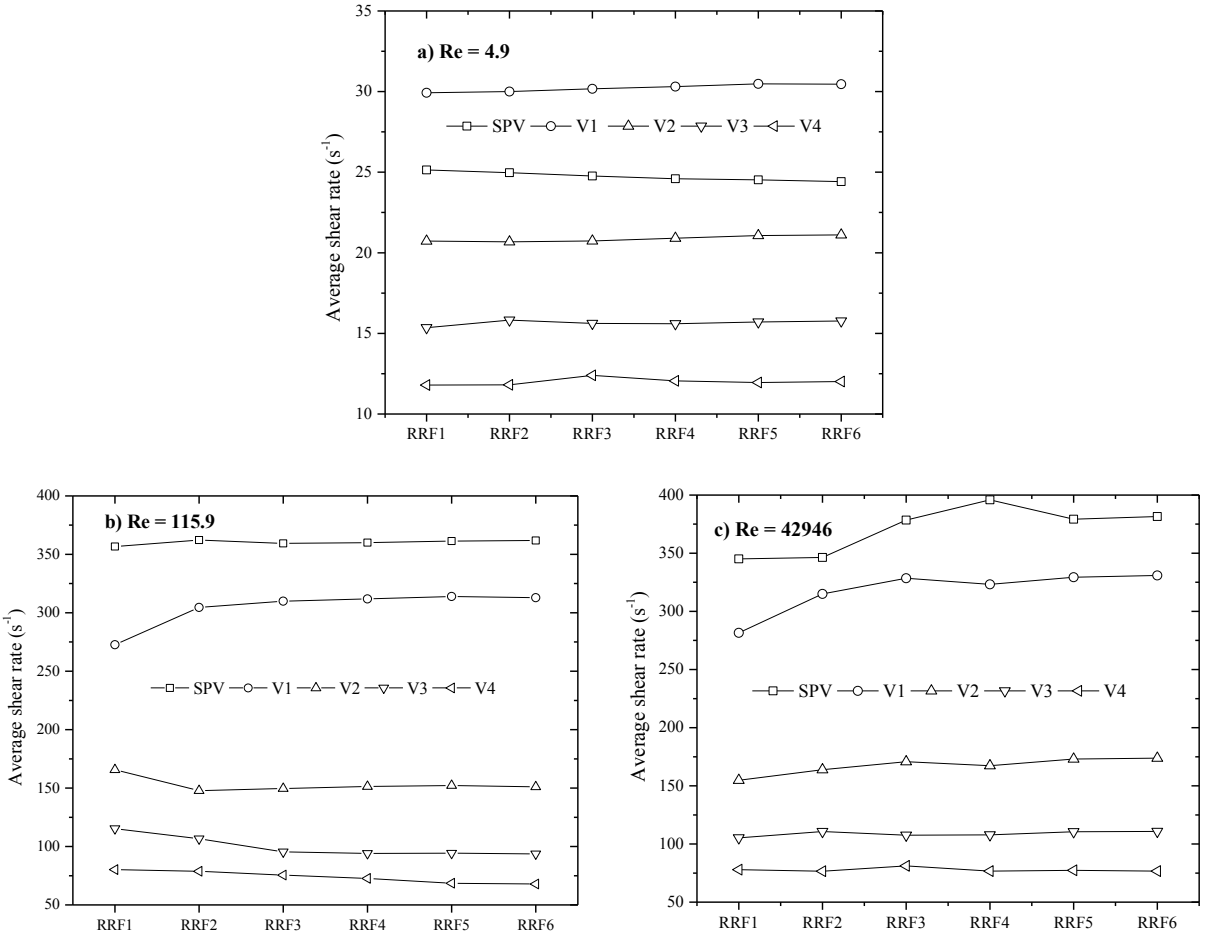

Fig. 8. Average shear rate values in volumes near the impeller as a function of the size of the RRF region for: a) Re=4.9, b) Re=115.9 and c) Re=42946.

3.4 Case study: Experimental system previously reported

In order to test our CFD results with respect to the appropriate extent of the RRF region for a stirred tank operating at fully turbulent conditions, an additional CFD model of an experimental agitation system published by Suzukawa, Kato, *et al*., (2006); Suzukawa, Mochizuki, *et al*., (2006), was reproduced. They carried out a study of turbines with four flat blades with four different attack angles, 45°, 60°, 75° and 90°, respectively. By synchronizing Laser-Doppler velocimetry with a rotary encoder coupled to the impeller shaft spinning clockwise, they collected readings of the mean velocity components for the impeller blade passage over an angle span of 90º between two neighboring baffles. However, for the purpose of this study, only the computational mesh with a blade angle attack of 90º and with the impeller blade halfway along the arc between the baffles was considered.

Information on the experimental setup can be found in the references of Suzukawa, Kato, *et al*., (2006); Suzukawa, Mochizuki, *et al*., (2006), and only relevant details in the context of this work are indicated below. The system investigated was a flat bottom cylindrical vessel equipped with four equally-spaced vertical baffles of width J = T/10, with no gap between the vessel wall and each baffle. These authors used ratios C/T=D/T=0.5, Z/T=1, D/W=5, with T=490 mm and W=24.5 mm. This system was operated at an impeller rotational speed of 2 rev/sec, leading to a tip velocity of 1.54 $m{\cdot}s^{-1}$ and Re=1.2×10^5, corresponding to fully turbulent conditions.

Table 4. Comparison between numerical predictions and reported experimental data, Re=1.2×10^5.

Parameter evaluated	Experimental from Suzukawa et al., (2006)	Numerical from this work	% error
N_P	4.72	4.08	13.6
$Q/v_{tip}R^2$	0.974	0.993	2
v_θ/v_{tip}, x/R=0.49, y=0	0.41	0.43	4.9
v_θ/v_{tip}, x/R=0.82, y=0	0.42	0.437	4.1

The computational mesh resulting from the application of the previous considerations consisted of two fluid volumes comprised in the RRF, i.e., RRF=BSV+V1 in addition to the static SRF region. It is convenient to highlight that the choice of the extension of the RRF of this computational mesh is equivalent to RRF5, depicted in Fig. 2, i.e., radial and axial extensions of 1.54R and 1.47R were used (see Table 2).

A mesh independence analysis similar to that described in Sections 2.2 and 3.1 was carried out for this computational mesh. The grid resolution study was performed using five different conformal grid sizes, ranging from 808655 to 5384051 cells. It was found that a grid with 3530199 cells was the most adequate and was therefore used in the computations. This independent mesh consisted of 393046 elements in the BSV zone, 776102 elements in V1 and 2361051 in the SRF. For this analysis, all meshes generated showed a skewness not greater than 0.89. The numerical considerations employed for simulations were the same as those described in Section 2.3 for turbulent flow regime.

In Table 4 our simulation results and the experimental data reported by Suzukawa, Mochizuki, *et al*. (2006) and Suzukawa, Kato, *et al*. (2006) are compared. These data consist of the dimensionless tangential velocity component (v_θ) at the impeller mid-plane (y=0) at two radial distances x_1/R =0.49 and x_2/R =0.816 when the impeller blade is positioned halfway between two immediate baffles (Suzukawa, Kato, *et al*., 2006). Also, the N_P and dimensionless values of the flow induced by the impeller [$Q/(v_{tip}R^2)$] (Suzukawa, Mochizuki, *et al*., 2006) are compared. The flow induced by the impeller (Q) through an extra cylinder-like surface surrounding it was calculated according to Suzukawa, Mochizuki, *et al*., (2006) as:

$$Q = 4\,[2\pi(R+2.5)] \int_{y=-25mm}^{y=25mm} v_r\, dy \qquad (12)$$

The factor four in Eq. (2) was included to account for the system periodicity.

As can be seen in Table 4, there is reasonable agreement between simulation results and experimental measurements of N_p, $Q/(v_{tip}R^2)$ and dimensionless local tangential velocities evaluated in the blade-swept region. The reliable numerical results obtained for this real agitated system corroborate that the dimensions employed for the RRF region, as well as the numerical considerations followed for CFD simulations, are adequate to predict the hydrodynamic evaluated parameters.

Conclusions

A CFD study was conducted to evaluate the effect of the interface position between the rotating and static reference frames on power number values and local velocity profiles, in multiple reference frame simulations of a baffled-tank equipped with a four flat blades turbine. To this end, six different volumes of the rotating domain surrounding the impeller were defined in the computational mesh. The study was carried out in the laminar and turbulent flow regimes.

It was found that at the lowest Reynolds number evaluated (Re=4.9) there is no significant effect of the size of the rotating domain on numerical results. However, as the Re increases, i.e., Re≥29.4, size plays an increasingly significant role. According to our results, the extension of the rotating domain is dependent on the flow regime, i.e., as the Re increases, its extension has to be enlarged to improve reliability of the numerical results. For the grid densities of the computational meshes evaluated in this study, the results obtained show that numerical values of power number and local velocity profiles are more sensitive to changes in the extension of the rotating domain than to the increase in the number of elements of the meshes.

The methodology used in this work might be employed as a selection criterion for the appropriate size of the rotating domain for other impeller types, e.g., mixed (pitched blade) or axial (hydrofoils) flow

impellers, which induce a predominant axial flow, instead of the radial flow for the impeller studied in this work. However, numerical studies of these impellers should be addressed with more detail in future works.

Acknowledgements

ADCG and VEMB thank Universidad Autónoma Metropolitana (Mexico) and Consejo Nacional de Ciencia y Tecnología.

Nomenclature

C	impeller off-bottom clearance [mm]
$C_{1\varepsilon}, C_{2\varepsilon}, C_{\mu}$	$\kappa-\varepsilon$ model constants [–]
D	impeller diameter [mm]
F_{cent}	centrifugal force [N·m^{-3}]
F_{cor}	Coriolis force [N·m^{-3}]
G_{κ}	generation of κ
J	baffle width [mm]
N	impeller speed [s^{-1}]
N_p	power number [–]
Q	pumping capacity [m$^3\cdot$ s^{-1}]
R	impeller radius [mm]
$\mathbf{r}$	location vector [m]
Re	Reynolds number [–]
T	tank diameter [mm]
$\mathbf{u}$	velocity vector [m·s^{-1}]
u_i, u_j	velocity components [m·s^{-1}]
V_{tip}	impeller tip velocity (m $\cdot$ seg^{-1})
$\overline{u}_i$	mean velocity [m·s^{-1}]
u_i'	instantaneous velocity [m·s^{-1}]
W	blade width [mm]
x, y, z	Cartesian coordinates [m]
Z	liquid height at rest [mm]

Abbreviations

ºBx	Brix degrees
BSV	Blades Swept Volume
CFD	Computational Fluid Dynamics
MRF	Multiple Reference Frame
RNG	Re-Normalization Group
rpm	Revolutions per minute
RRF	Rotating Reference Frame
RRF1 to RRF6	Different rotating reference frame regions
RSM	Reynolds Stress Turbulence Model
SM	Sliding Mesh
SRF	Static Reference Frame
SST	Shear Stress Turbulence
V1 to V6	Volumes of fluid around the impeller

Greek letters

ρ	density [kg ·m^{-3}]
$\Im$	torque [N·m]
μ	viscosity
μ_T	turbulent viscosity
ε	turbulent energy dissipation rate [m$^2\cdot$s^{-3}]
κ	turbulent kinetic energy [m$^2\cdot$s^{-2}]
ν	kinematic viscosity [m·s^{-1}]
$\sigma_{\kappa}, \sigma_{\varepsilon}$	$\kappa-\varepsilon$ model constants [–]
$\boldsymbol{\omega}$	angular velocity [s^{-1}]

References

Ameur, H. (2018). Modifications in the Rushton turbine for mixing viscoplastic fluids. *Journal of Food Engineering 233*, 117-125.

Ammar, M., Driss, Z., Chtourou, W., & Abid, M. S. (2012). Effect of the tank design on the flow pattern generated with a pitched blade turbine. *International Journal of Mechanical Engineering and Applications 2*, 12-19.

Brucato, A., Ciofalo, M., Grisafi, F., & Micale, G. (1998). Numerical prediction of flow fields in baffled stirred vessels: A comparison of alternative modelling approaches. *Chemical Engineering Science 53*, 3653-3684.

Brucato, A., Ciofalo, M., Grisafi, F., & Tocco, R. (2000). On the simulation of stirred tank reactors via computational fluid dynamics. *Chemical Engineering Science 55*, 291-302.

Chtourou, W., Ammar, M., Driss, Z., & Abid, M. S. (2014). CFD Prediction of the turbulent flow generated in stirred square tank by a Rushton turbine. *Energy and Power Engineering 6*, 6.

Deen, N. G., Solberg, T., & Hjertager, B. H. (2002). Flow generated by an aerated Rushton impeller: Two-phase PIV experiments and numerical simulations. *The Canadian Journal of Chemical Engineering 80*, 1-15.

Deglon, D. A., & Meyer, C. J. (2006). CFD modelling of stirred tanks: Numerical considerations. *Minerals Engineering 19*, 1059-1068.

Devi, T. T., Kumar, B., & Patel, A. K. (2015). Detached eddy simulation of turbulent flow in

stirred tank reactor. *Procedia Engineering 127*, 87-94.

Fathi Roudsari, S., Turcotte, G., Dhib, R., & Ein-Mozaffari, F. (2012). CFD modeling of the mixing of water in oil emulsions. *Computers & Chemical Engineering 45*, 124-136.

Fluent, A. (2015). *Theory Guide*. Ansys Inc.

Galindo, E., & Nienow, A. W. (1992). Mixing of highly viscous simulated xanthan fermentation broths with the lightnin A-315 impeller. *Biotechnology Progress 8*, 233-239.

Ghadge, R.S., Patwardhan, A.W., Sawant, S.B. & Joshi, J.B. (2005). Effect of flow pattern on cellulase deactivation in stirred tank bioreactors. *Chemical Engineering Science 60*, 1067-1083.

Gibbardo, B., Micale, G., Grisafi, F., B., & Ciofalo, M. (2006). Numerical simulation of low-reynolds flow fields in unbaffled stirred vessels. 12th European Conference on Mixing, Bologna.

Glover, G. M. C., & Fitzpatrick, J. J. (2007). Modelling vortex formation in an unbaffled stirred tank reactors. *Chemical Engineering Journal 127*, 11-22.

Joshi, J. B., Nere, N. K., Rane, C. V., Murthy, B. N., Mathpati, C. S., Patwardhan, A. W., & Ranade, V. V. (2011a). CFD simulation of stirred tanks: Comparison of turbulence models (Part II: Axial flow impellers, multiple impellers and multiphase dispersions). *The Canadian Journal of Chemical Engineering 89*, 754-816.

Joshi, J. B., Nere, N. K., Rane, C. V., Murthy, B. N., Mathpati, C. S., Patwardhan, A. W., & Ranade, V. V. (2011b). CFD simulation of stirred tanks: Comparison of turbulence models. Part I: Radial flow impellers. *The Canadian Journal of Chemical Engineering 89*, 23-82.

Kelly, W., & Gigas, B. (2003). Using CFD to predict the behavior of power law fluids near axial-flow impellers operating in the transitional flow regime. *Chemical Engineering Science 58*, 2141-2152.

Lane, G. L., Schwarz, M. P., & Evans, G. M. (2000). Chapter 34 - Comparison of CFD Methods for Modelling of Stirred Tanks. In H. E. A. van den Akker & J. J. Derksen (Eds.), 10th European Conference on Mixing (pp. 273-280). Amsterdam: Elsevier Science.

Lee, K. C., & Yianneskis, M. (1994). The extent of periodicity of the flow in vessels stirred by Rushton impellers. *AIChE Symposium Series 9*, 5-18.

Luo, J. Y., Issa, R.I., Gosman, A.D. (1994). Prediction of impeller-induced flows in mixing vessels using multiple frames of reference. Eighth European Conference on Mixing, 136.

McFarlane, C.M. & Nienow, A.W. (1995). Studies of high solidity ratio hydrofoil impellers for aerated bioreactors. 1. Review. *AIChE Journal 11*, 601-607.

Márquez-Baños, V. E., De La Concha-Gómez, A. D., Valencia-López, J. J., López-Yáñez, A., & Ramírez-Muñoz, J. (2019). Shear rate and direct numerical calculation of the Metzner-Otto constant for a pitched blade turbine. *Journal of Food Engineering 257*, 10-18.

Mendoza, F., Bañales, A. L., Cid, E., Xuereb, C., Poux, M., Fletcher, D. F., & Aubin, J. (2018). Hydrodynamics in a stirred tank in the transitional flow regime. *Chemical Engineering Research and Design 132*, 865-880.

Murthy, B. N., & Joshi, J. B. (2008). Assessment of standard $\kappa - \varepsilon$, RSM and LES turbulence models in a baffled stirred vessel agitated by various impeller designs. *Chemical Engineering Science 63*, 5468-5495.

Murthy, J. Y., Mathur, S. R., & Choudhury, C. (1994). CFD simulation of flow in stirred tanks reactor using a sliding mesh technique. Eighth European Conference on Mixing 136, 341-345.

Oshinowo, L., Jaworski, Z., Dyster, K. N., Marshall, E., & Nienow, A. W. (2000). Chapter 35 - Predicting the tangential velocity field in stirred tanks using the Multiple Reference Frames (MRF) model with validation by LDA measurements. In H. E. A. van den Akker & J. J. Derksen (Eds.), *10th European Conference on Mixing* (pp. 281-288). Amsterdam: Elsevier Science.

Pakzad, L., Ein-Mozaffari, F., Upreti, S. R., & Lohi, A. (2013). Characterisation of the mixing of non-newtonian fluids with a scaba 6SRGT

impeller through ert and CFD. *The Canadian Journal of Chemical Engineering 91*, 90-100.

Patton, T. C. (1979). *Paint Flow and Pigment Dispersion* (2 ed.). New York: Wiley Interscience Publishers.

Paul, E. L., Atlemo-Obeng, V. A., & Kresta, S. M. (2004). *Handbook of Industrial Mixing* (W. Interscience Ed. Vol. 8). New Jersey: American Chemical Society.

Perry, R. H., & Green, D. W. (2008). *Perry's Chemical Engineers' Handbook*. New York: McGraw-Hill.

Pope, S. B. (2000). *Turbulent Flows*. Cambridge University Press, Cambridge, UK.

Raffo-Durán, J., Figueredo-Cardero, A., & Dustet-Mendoza, J.C. (2014). Características de la hidrodinámica de un biorreactor industrial tipo tanque agitado. *Revista Mexicana de Ingeniería Química 13*, 823-839.

Rahimi, M., Kakekhani, A., & Alsairafi, A. A. (2010). Experimental and computational fluid dynamic (CFD) studies on mixing characteristics of a modified helical ribbon impeller. *Korean Journal of Chemical Engineering 27*, 1150-1158.

Ramírez-Gómez, R., García-Cortés, D., Martínez-de Jesús, G., González-Brambila, M. M., Alonso, A., Martínez-Delgadillo, S. A., & Ramírez-Muñoz, J. (2015). Performance evaluation of two high-shear impellers in an unbaffled stirred tank. *Chemical Engineering & Technology 38*, 1519-1529.

Ramírez-Muñoz, J., Guadarrama-Pérez, R., & Márquez-Baños, V. E. (2017). A direct calculation method of the Metzner-Otto constant by using computational fluid dynamics. *Chemical Engineering Science 174*, 347-353.

Ramírez-Muñoz, J., Martínez-de-Jesús, G., Soria, A., Alonso, A., & Torres, L. G. (2016). Assessment of the effective viscous dissipation for deagglomeration processes induced by a high shear impeller in a stirred tank. *Advanced Powder Technology 27*, 1885-1897.

Rushton, J., & Oldshue, J. (1953). Mixing present theory and practice. *Chemical Engineering Progress 49*, 161-168.

Sommerfeld, M., & Decker, S. (2004). State of the art and future trends in CFD simulation of stirred vessel hydrodynamics. *Chemical Engineering & Technology 27*, 215-224.

Sossa-Echeverria, J., & Taghipour, F. (2012). Mixing of Newtonian and Non-Newtonian fluids in a cylindrical mixer equipped with a side-entry impeller. *Industrial & Engineering Chemistry Research 51*, 15258-15267.

Suzukawa, K., Kato, K., Mochizuki, S., & Osaka, H. (2006). Vortex Structures around a flat paddle impeller in a stirred vessel. *JSME International Journal 49*, 426-433.

Suzukawa, K., Mochizuki, S., & Osaka, H. (2006). Effect of the attack angle on the roll and trailing vortex structures in an agitated vessel with a paddle impeller. *Chemical Engineering Science 61*, 2791-2798.

Tamburini, A., Gagliano, G., Micale, G., Brucato, A., Scargiali, F., & Ciofalo, M. (2018). Direct numerical simulations of creeping to early turbulent flow in unbaffled and baffled stirred tanks. *Chemical Engineering Science 192*, 161-175.

Van den Akker, H. E. A. (2006). The details of turbulent mixing process and their simulation. In G. B. Marin (Ed.), *Advances in Chemical Engineering 31*, 151-229, Academic Press.

Walters, D. K., & Cokljat, D. (2008). A three-equation eddy-viscosity model for Reynolds-averaged Navier-Stokes simulations of transitional flow. *Journal of Fluids Engineering 130*, 121401-121401-121414.

Wechsler, K., Breuer, M., & Durst, F. (1999). Steady and unsteady computations of turbulent flows induced by a 4/45° pitched-blade impeller. *Journal of Fluids Engineering 121*, 318-329.

Wu, H., Patterson, G.K. (1989). Laser-Doppler measurements of turbulent-flow parameters in a stirred mixer. *Chemical Engineering Science 44*, 2207-2221.

Zadravec, M., Ba?i?, S., & Hriber?ek, M. (2007). The influence of rotating domain size in a rotating frame of reference approach for simulation of rotating impeller in a mixing vessel. *JESTECH 2*, 126-138.

Zalc, J. M., Alvarez, M. M., Muzzio, F. J., & Arik, B. E. (2001). Extensive validation of computed laminar flow in a stirred tank with three Rushton turbines. *AIChE Journal 47*, 2144-2154.